The influence of cavern length on deformation and barrier integrity around horizontal energy storage salt caverns

Jinlong Li[a,b], Ning Zhang[c,b,*], Wenjie Xu[a], Dmitri Naumov[b], Thomas Fischer[d], Yunmin Chen[a], Duanyang Zhuang[a,*], Thomas Nagel[b,a]

[a] *MOE Key Laboratory of Soft Soils and Geoenvironmental Engineering, Hypergravity Research Center of Zhejiang University (HRC-ZJU), Zhejiang University, Yuhangtang Rd 866, Hangzhou, 310058, Zhejiang, China*
[b] *Geotechnical Institute, Technische Universität Bergakademie Freiberg, Gustav-Zeuner-Straße 1, Freiberg, 09599, Sachsen, Germany*
[c] *School of Science, Nanjing Univerity of Science and Technology, Xiaolingwei 200, Nanjing, 210094, Jiangsu, China*
[d] *Department of Environmental Informatics, Helmholtz Centre for Environmental Research – UFZ, Permoserstraße 15, Leipzig, 04318, Sachsen, Germany*

Abstract

Horizontal cavern structures are discussed as a means to constructing energy storage facilities in bedded salt formations. During their design, the spacing of injection and discharge boreholes for solution mining is an important variable determining cavern length, shape and construction cost. Increasing the borehole spacing has been suggested in order to increase cavern capacity and construction rate while decreasing construction cost but its mechanical consequences have yet to be explored. In this paper, cavern geometries constructed with different borehole spacings are obtained using a solution mining simulation model. Static creep analyses have been conducted based on these geometrical models to discuss the impact of the borehole spacing on the mechanical behavior of the caverns. The results show that the creep deformation of the horizontal cavern induces limited volume change depending on operating pressures. Increasing the borehole spacing initially increases cavern roof displacement and volumetric convergence, but plateaus after a distance 600m, i.e. 5-6 times the cross-sectional diameter. A similar behavior

*Corresponding author `zhangning@mail.njust.edu.cn;zhuangdy@zju.edu.cn`

is observed in terms of selected integrity criteria. The results indicate the principal possibility to access larger storage volumes and higher construction speed by increasing the borehole spacing to longer than 5-6 times the designed cross-sectional diameter.

Keywords: Salt cavern, energy storage, solution mining, stability, creep, OpenGeoSys

---

Nomenclature

Greek Symbols

Symbol	*Description*	*Unit*
$\boldsymbol{\epsilon}$	Strain tensor	–
$\boldsymbol{\epsilon}^{\mathrm{cr}}$	Creep strain tensor	–
$\boldsymbol{\epsilon}^{\mathrm{el}}$	Elastic strain tensor	–
$\boldsymbol{\epsilon}^{\mathrm{th}}$	Thermal strain tensor	–
$\boldsymbol{\sigma}$	Stress tensor	MPa
$\boldsymbol{\mathcal{C}}$	Fourth-order stiffness tensor	MPa
λ	First Lamé constant	MPa
μ	Second Lamé constant	MPa
ν	Poisson's ratio	–
ρ	Bulk mass density	$\mathrm{kg\,m^{-3}}$
σ^{t}	Tensile strength	MPa
σ_{ref}	Reference stress	MPa
σ_i	Principal stresses ($i \in \{1, 2, 3\}$	MPa
τ_{oct}	Octahedral shear stress	MPa

φ	Angle of internal friction	$^\circ$

Operators

Symbol	*Description*	*Unit*
$:$	Double contraction	–
$\dot{(\,)}$	Material time derivative	–
$\odot$	A symmetric tensor product operator	–
$\otimes$	Dyadic product operator	–
tr	Trace of a tensor	–

Roman Symbols

Symbol	*Description*	*Unit*
$\boldsymbol{\mathcal{I}}$	Fourth-order identity tensor	–
$\mathbf{I}$	Second-order identity tensor	–
$\mathbf{s}$	Deviatoric stress tensor	MPa
A	Creep coefficient in BGRa model	1/a
c	Cohesion	MPa
E	Young's modulus	GPa
G	Shear modulus	GPa
m	Creep exponent in BGRa model	–
Q	Activation energy	J/mol

1. Introduction

Underground salt caverns have been widely used for energy storage since the 1940's [1, 2]. Nowadays, there are more than 90 salt cavern underground gas storage sites in the world, with a daily working gas volume of about $1.56 \cdot 10^{10}\,\mathrm{m}^3$ accounting for about $23\,\%$ of the total working gas volume of all kinds of underground gas storage [3]. About $66\,\%$ of the strategic petroleum reserve is stored in salt caverns worldwide [4, 5]. Moreover, there is a considerable number of studies related to the storage of H_2, CO_2 and compressed air in salt caverns [6, 7, 8, 9]. Using salt caverns for toxic or nuclear waste disposal has been reported as well [10, 11].

Usually, salt caverns are mostly solution mined vertical structures [12] which are constructed in salt domes [13], where the height of the vertical cavern can reach $400\,\mathrm{m}$ to $600\,\mathrm{m}$, and the volume can reach 2 million m^3. However, as salt domes are not available in all locations and are increasingly exploited, more attention is being paid to bedded salt formations which are more widely distributed around the world, *e.g.* China, Canada, Poland, Germany and the US[14, 15]. Such bedded salt formations are comparatively thin and often contain many insoluble interlayers [16, 2, 17]. Due to their different geological evolution, the mechanical properties of domal and bedded salt formations also differ with consequences for stability and tightness assessment [18]. Due to geometrical constraints and the layered structure, the construction of vertical salt caverns can be very difficult in these formations. Particularly, the insoluble interlayers will result in irregularities and reduce the cavern capacity. In China, most vertical salt caverns are lower than 120 meters and thus comparatively shallow, and their volume usually does not exceed $200\,000\,\mathrm{m}^3$. The construction costs are higher as well, since more drilling operations are required in order to obtain a volume comparable to that of one large cavern in a salt dome. To obtain a larger cavern capacity at lower cost, a two-well horizontal cavern construction method has been proposed [19]. The horizontal cavern uses two boreholes for alternate water injection and brine discharge [20, 21, 22]. As the injected fresh water is lighter than the brine and will rise up very quickly [23, 24], primarily the salt around the injection point will be dissolved. To extend the solution process to the central part of the horizontal cavern, the injection tube is usually designed in a retractable configuration [25]. In the beginning, the injection tube orifice is placed close to the discharge borehole through the injection borehole. A cavern appears near the discharge borehole due to the water injection and salt dissolution. During the subsequent stages, the injection tube is retracted step by step and gets closer to the injection borehole. Caverns grow around the retracting injection tube's origin borehole[20]. At that stage, a horizontal tunnel-like cavern will have developed with a shape reminiscent of candied fruit. The recorded length of a horizontal cavern can reach 150 m to 500 m [21]. With such horizontal caverns, larger volumes can be obtained than with vertical caverns in bedded salt formations [26]. Due to the larger dissolution area, its construction efficiency is higher than a vertical cavern as well [20]. It has been widely accepted that the horizontal cavern is more suitable for developing larger storage caverns in bedded salt in China [8, 20, 27, 28].

To ensure safe and economic storage of gas or oil, the cavern should be carefully designed to minimize its convergence rate and deformation of the surrounding rock mass and to limit the size of surrounding plastic zones in which dilatancy may enhance permeability [21, 29]. One of the most important design parameters of a horizontal cavern is the distance between the two boreholes drilled for water injection and brine discharge, or "borehole spacing" for short. This distance controls the total length and volume of the cavern. Solution mining of a group of horizontal caverns was simulated with increasing borehole spacing by Li *et al.* [28]. The results show that the capacity of a horizontal cavern in a fixed salt formation can be higher than a vertical cavern, and it increases with the borehole spacing of the cavern. In addition, a longer horizontal cavern has a larger dissolution area and thus a higher construction efficiency (dissolution rate). The consumption of fresh water and energy per volume are lower as well [28]. However, according to research by Chen *et al.* [29], the vertical displacement of the cavern roof and the volume loss might increase with the aspect ratio of a salt cavern, which indicates that the borehole spacing of a horizontal cavern might be subject to an upper limit. The maximum length of the salt cavern was limited to about 120 m in the research by Chen *et al.* [29] and cannot be directly used for the design of two-well horizontal caverns which are usually longer than 200 m.

There have been many studies concerning the mechanical behavior and long-term stability of a horizontal cavern for gas and oil storage. Xing *et al.* [27, 30] conducted a comparison of the mechanical behavior of vertical and horizontal salt caverns and showed that a $200 \times 100 \times 70\,\mathrm{m}^3$ horizontal cavern can meet all the design criteria for long-term operation of storage caverns. Liu *et al.* [21, 8] dissolved a horizontal model cavern in the laboratory. Based on the obtained cavern shape, three caverns with top-enlarged, middle-enlarged and bottom-enlarged structures were assumed and analyzed mechanically. The top-enlarged cavern was demonstrated to posses the best serviceability and safety. Chen *et al.* [29] have conducted research on small-space two-well salt caverns and discussed the impact of the width-to-height ratio and inner gas pressure on the cavern stability.

Most previous studies have been discussing the reliability of the horizontal salt cavern by comparing horizontal and vertical caverns, or by comparing different forms of horizontal cavities. However, discussions on the impact of the length of horizontal salt caverns on their stability have not been presented. In addition, shapes derived from sonar mapping suffer some limitations in horizontal caverns, due to some blockage of the long horizontal tunnel by insoluble sediments. Thus, several aspects of cavern morphology remain unknown in bedded salt. Therefore, in most previous studies, a hypothetical morphology was mostly used for the mechanical analysis [8, 21, 27, 29, 30], which could only be qualitative but not quantitative.

In this paper, the impact of borehole spacing on the stability of the cavern is discussed to optimize the parameter design and hence profitability while maintaining the necessary safety of storage caverns. A series of cavern geometries with different borehole spacing and cavern length is obtained using a construction modeling program of Li *et al.* [28]. Then 3D geomechanical models are set up based on these geometries in the open-source finite element framework OpenGeoSys [31] and analyzed using the software's high-performance computing features. The volumetric convergence ratio, cavern roof displacement and extent of plastic zones are compared and discussed to evaluate the mechanical performance of caverns with different borehole spacing. The results provide insights into the construction and design of horizontal salt caverns.

2. Numerical model of horizontal salt caverns for combined dissolution and geomechanical analysis

2.1. Solution mining model

A solution mining model has been proposed by Li *et al.* [28] to design cavern construction protocols. The dissolution rate of the salt has been considered as mainly related to the angle of the brine-salt interface, the flow rate and concentration of the brine, and the content of the insoluble substances. The angle of the brine-salt interface can be easily calculated from the cavern geometry, and the content of the insoluble substances can be accessed through geological exploration. Thus, the flow rate and concentration of the brine remain as key factors to be determined. A simplified flow/concentration model is used for the efficient solution of the 3D turbulent flow/concentration fields. The brine concentration around the injection point is considered as homogeneous as in a vertical cavern, due to the blending of the upward flow of the injected fresh water with the downward flow of saturated brine from the salt dissolution. In long horizontal tunnel-like structures, the brine is assumed to flow along the horizontal direction only, while vertical flow and vertical concentration gradients are neglected. The dissolved salt is considered to be evenly dispersed into the solution. Using these assumptions, the dynamic flow and concentration fields of the brine in the entire cavern are solved based on the laws of conservation of mass and momentum. Thus, the dissolution rate of the salt boundary can be calculated and the shape of the salt cavern predicted. This model has been implemented into a softwaren named "Multi-Step Horizontal Salt Cavern Leaching Simulation" (M-SHSCLS), the reliability of which has been validated by comparison with field data[28].

Using this program, a total of 11 horizontal salt cavern geometries constructed virtually based on different borehole spacings ranging from 200 m to 1200 m have been obtained (Figure 1). The retraction distances of the injection point are all 100 m in these simulations, thus the number of the retraction steps during the construction phase ranges from 2 to 12. In each step, a sub-cavern forms around the injection point due to the salt dissolution by the buoyant flow of the injected fresh water. The final shape consists of several sub-caverns, the number of which increases with the length of the horizontal borehole (i.e. the spacing between the corresponding vertical boreholes). The volume and height of these cavern peaks are similar since the time and injection flow rate between the retraction steps remain fixed.

Comparing with the conventional vertical salt cavern shown in Figure 2, the horizontal cavern is more suitable for the geological structure of bedded salt in China. With the horizontal dissolution model, large volume caverns comparable to their vertical counterparts in the salt domes could be obtained provided roof heights essential for safety. If moderate deformation and prolonged barrier integrity around horizontal caverns could be demonstrated, this dissolution approach could largely increase the efficiency of the construction and reduce the investment required for energy storage in China.

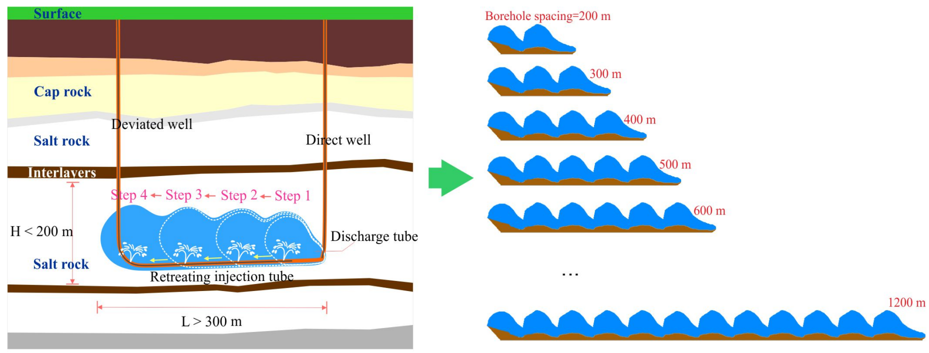

Figure 1: Multi-step horizontal cavern solution mining model proposed by Li *et al.* [28]

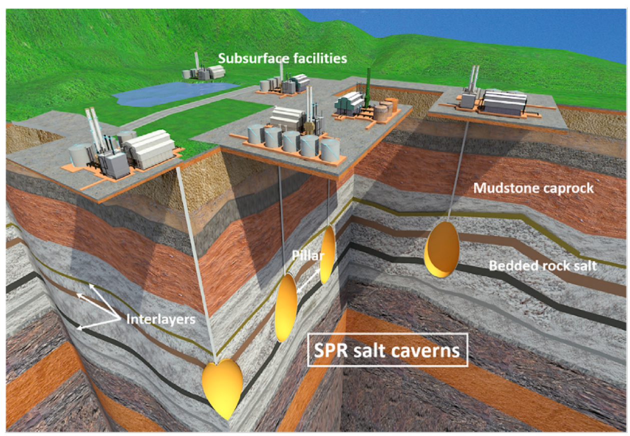

Figure 2: Conventional vertical salt cavern model [5]

2.2. Geomechanical model

The first salt mine developed for natural gas storage in China is located in Jintan [32]. There, more than 20 caverns have been constructed and an energy storage site is in operation. After long-term investigation, research, and construction, its geological parameters have been well investigated. Also, it is a potential test site for horizontal salt caverns, motivating its use as a representative site for the mechanical simulation of horizontal salt caverns in this paper. The depth range of the numerical model is between −550 m and −1550 m, with a 200 m thick salt layer ranging from −950 m to −1150 m embedded between two mudstone layers. The roof of the salt formation is composed of ash mudstone and silty mudstone layers with a thickness of about 400 m. The bottom of the salt formation is a dense silty mudstone

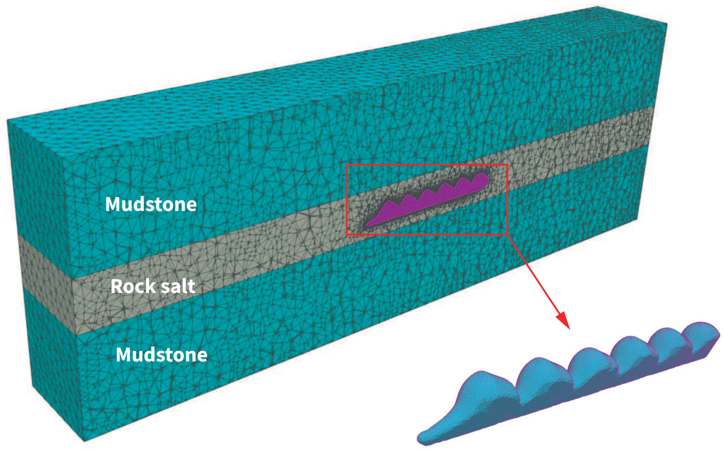

Figure 3: An example of a FEM model of a 600 m long cavern.

layer with a thickness of more than 100 m. A total 11 horizontal salt cavern geometries with different borehole spacings (200 m to 1200 m) are modeled based on the approach described in subsection 2.1 and Li *et al.* [28]. The height and with of the caverns are about 120 m and 100 m, respectively. To avoid unwanted boundary effects, a large domain size with a length of 3000 m, a width of 1000 m and a height of 1000 m is chosen for the geomechanical simulations, extending the thickness of the bottom mud stone layer to 400 m as well. The caverns with different lengths are placed in the center of the model, as shown in Figure 3. The geometric models are meshed with linear tetrahedral elements using GMSH[33]. To accommodate both accuracy and the efficiency requirements, the boundary of the model is meshed with a relatively large maximum element edge length of about 50 m, while the mesh around cavern uses a higher resolution with maximum element edge lengths from 6 m to 9 m, resulting in models with 225 176 to 276 503 elements. This resulted in 155 652 to 188 730 degrees of freedom. Static creep analyses have been conducted based on these geometrical models with the open-source code OpenGeoSys (OGS) [34, 31] based on the Finite Element Method (FEM).

2.2.1. Constitutive model

Salt rock exhibits pronounced time-dependent deformation or creep under relatively low stress level and has very low permeability and porosity [35, 36]. To evaluate the deformation and barrier integrity of the salt rock energy storage caverns, a suitable constitutive model is required. The initial transient creep phase of rock salt only lasts for several months, which is shorter than the construction stage[21, 8]. The mechanical simulation here starts after the cavern has been constructed. We further limited ourselves to static gas pressures. Thus, transient creep phenomena were ignored, and a steady-state creep law was used. To capture stationary creep under non-isothermal conditions the BGRa [37, 36] model is used. The BGRa model has been introduced[37] to describe the steady-state creep deformation of rock salt as a function of temperature and stress based on Orowan's law [38], which has been tested and successfully applied to rock salt storage and disposal projects [39, 36]. In the BGRa model, the creep strain rate is described as

$$\dot{\boldsymbol{\epsilon}}^{\mathrm{cr}} = \sqrt{\frac{3}{2}} A e^{-Q/(RT)} \left(\frac{\bar{\sigma}}{\sigma_{\mathrm{ref}}}\right)^m \frac{\mathbf{s}}{\|\mathbf{s}\|}, \tag{1}$$

where $\mathbf{s} = \boldsymbol{\sigma} - \frac{1}{3}\mathrm{tr}(\boldsymbol{\sigma})\mathbf{I}$ is the deviatoric stress and $\bar{\sigma}$ denotes the von Mises equivalent stress defined as $\bar{\sigma} = \sqrt{\frac{3}{2}}\|\mathbf{s}\|$.

Equivalently, the creep strain rate can be written as

$$\dot{\boldsymbol{\epsilon}}^{\mathrm{cr}} = b\|\mathbf{s}\|^{m-1}\mathbf{s} \tag{2}$$

by introducing

$$b = \left(\frac{3}{2}\right)^{(m+1)/2} \frac{A e^{-Q/(RT)}}{\sigma_{\mathrm{ref}}^m}. \tag{3}$$

The total strain rate considering creep and thermal strains is

$$\dot{\boldsymbol{\epsilon}} = \dot{\boldsymbol{\epsilon}}^{\mathrm{el}} + \dot{\boldsymbol{\epsilon}}^{\mathrm{th}} + \dot{\boldsymbol{\epsilon}}^{\mathrm{cr}}, \tag{4}$$

where $\dot{\boldsymbol{\epsilon}}^{\mathrm{el}}$ is the elastic strain rate, $\dot{\boldsymbol{\epsilon}}^{\mathrm{th}}$ is the thermal strain rate, and $\dot{\boldsymbol{\epsilon}}^{\mathrm{cr}}$ is the creep strain rate.

Following Hooke's law, the stress rate is given by

$$\dot{\boldsymbol{\sigma}} = \boldsymbol{\mathcal{C}}{:}\dot{\boldsymbol{\epsilon}}^{\mathrm{el}} = \boldsymbol{\mathcal{C}}{:}(\dot{\boldsymbol{\epsilon}} - \dot{\boldsymbol{\epsilon}}^{\mathrm{th}} - \dot{\boldsymbol{\epsilon}}^{\mathrm{cr}}), \tag{5}$$

where $\boldsymbol{\mathcal{C}} = \lambda\boldsymbol{\mathcal{I}} + 2G\mathbf{I}\odot\mathbf{I}$ is the fourth-order elastic stiffness tensor for linearly elastic isotropic media. Substituting Eq. (2) and $\boldsymbol{\mathcal{C}}$ into the stress rate equation, yields

$$\dot{\boldsymbol{\sigma}} = \boldsymbol{\mathcal{C}}{:}(\dot{\boldsymbol{\epsilon}} - \dot{\boldsymbol{\epsilon}}^{\mathrm{th}}) - 2bG\|\mathbf{s}\|^{m-1}\mathbf{s}. \tag{6}$$

OpenGeoSys uses an implicit time integration scheme [40, 41, 42] to obtain the stress in the current time step, $n+1$, which can here be expressed as

$$\boldsymbol{\sigma}^{n+1} = \boldsymbol{\sigma}^n + \boldsymbol{\mathcal{C}}{:}(\Delta\boldsymbol{\epsilon} - \alpha_T \Delta T \mathbf{I}) - 2bG\Delta t \left\|\mathbf{s}^{n+1}\right\|^{m-1} \mathbf{s}^{n+1} \tag{7}$$

with α_T being the linear thermal expansion coefficient and Δ the increment of a quantity over the current time step.

To solve for stress, the Newton-Raphson scheme is applied. Let

$$\mathbf{r} = \boldsymbol{\sigma}^{n+1} - \boldsymbol{\sigma}^n - \boldsymbol{\mathcal{C}}(\Delta\boldsymbol{\epsilon} - \alpha_T \Delta T \mathbf{I}) + 2bG\Delta t \left\|\mathbf{s}^{n+1}\right\|^{m-1} \mathbf{s}^{n+1} \tag{8}$$

be the residual for the stress equation. The Jacobian of is derived as

$$\begin{aligned}\mathbf{J}_{\boldsymbol{\sigma}} &= \frac{\partial \mathbf{r}}{\partial \boldsymbol{\sigma}^{n+1}} \\ &= \boldsymbol{\mathcal{I}} + 2bG\Delta t \left\|\mathbf{s}^{n+1}\right\|^{m-1} \left(\boldsymbol{\mathcal{I}} - \frac{1}{3}\mathbf{I} \otimes \mathbf{I} + (m-1)\left\|\mathbf{s}^{n+1}\right\|^{-2} \mathbf{s}^{n+1} \otimes \mathbf{s}^{n+1}\right).\end{aligned} \tag{9}$$

Once the stress integration is converged, the consistent tangent operator is obtained from [43]

$$\frac{\partial \Delta\boldsymbol{\sigma}^{n+1}}{\partial \Delta\boldsymbol{\epsilon}^{n+1}} = \mathbf{J}_{\boldsymbol{\sigma}}^{-1} \boldsymbol{\mathcal{C}} \tag{10}$$

Since this study focuses on an initial assessment of long-term creep effects, an isothermal setting was considered. Therefore, $\dot{\boldsymbol{\epsilon}}^{\mathrm{th}} = \mathbf{0}$, and the temperature-dependent creep law-coefficient has been redefined by eliminating the Arrhenius term evaluated at a fixed temperature:

$$A \leftarrow A \exp\left(-\frac{Q}{RT_0}\right) \tag{11}$$

where $T_0 = 293.17\,\mathrm{K}$ is the in-situ temperature and $Q = 54\,\mathrm{kJ\,mol^{-1}}$. Therefore, the expression for b simplifies to

$$b = \left(\frac{3}{2}\right)^{(m+1)/2} \frac{A}{\sigma_{\mathrm{ref}}^m}. \tag{12}$$

Mudstone does not exhibit significant creep and the Mohr-Coulomb model is frequently used to model its elasto-plastic behavior [44, 45]. Here, plastic deformations in the mudstone layers are not considered during the simulations, so they were represented as elastic materials.

	ρ / $\mathrm{kg\,m^{-3}}$	E / GPa	ν	A / $\mathrm{a^{-1}}$	n	c / MPa	φ / °	σ^{t} / MPa
Rock salt	2220	3.99	0.24	1.5×10^{-6}	4.48	1.0	35	1.0
Mudstone	2310	3.5	0.175	-	-	1.0	30	1.0

Table 1: Parameters of rock salt and mudstone.

The parameters of rock salt and mudstone are given by Table 1 [46]. The given strength parameters were not used in the constitutive model per se but only in the analysis of the simulation results.

2.2.2. Integrity criteria

A number of mechanical criteria are typically used to assess the long-term stability of salt structures such as mines or caverns. Among them, the two most prevalent are the dilatancy criterion and the fluid pressure criterion [47, 48] (equivalent to the no effective tensile stress criterion). The latter criterion is here expressed as

$$F_{\mathrm{p}} = p_{\mathrm{L}} - \sigma_{\mathrm{min}}, \tag{13}$$

where p_{L} is a hydrostatic pressure resulting from a hypothetical water column to the considered depth, and σ_{min} is the least compressive principal stress (compression positive). $F_{\mathrm{p}} \geq 0$ implies failure. In the present case, the hypothetical water column is given as

$$p_{\mathrm{L}} = \rho_{\mathrm{L}} g z. \tag{14}$$

The dilatancy criterion is sometimes evaluated in terms of total stresses $\boldsymbol{\sigma}$, sometimes in terms of effective stresses $\boldsymbol{\sigma}'$ assuming a hypothetical water column from the ground surface similar to the previous criterion. Here, we use the dilatancy boundary following Cristescu und Hunsche employed in [49, 47]

$$\frac{\tau_{\mathrm{f}}}{\sigma^*} = a \cdot \left(\frac{\sigma_{\mathrm{m}}}{\sigma^*}\right)^2 + b \cdot \left(\frac{\sigma_{\mathrm{m}}}{\sigma^*}\right), \tag{15}$$

$$\frac{\tau_{\mathrm{f}}}{\sigma^*} = a \cdot \left(\frac{\sigma'_{\mathrm{m}}}{\sigma^*}\right)^2 + b \cdot \left(\frac{\sigma'_{\mathrm{m}}}{\sigma^*}\right), \tag{16}$$

where $\sigma^* = 1\,\mathrm{MPa}$ and the parameters $a = -0.0123$, $b = 0.7731$ have been fitted to data from Ma *et al.* [50] to represent the material considered in this study.

The dilatancy criterion is given as

$$F_{\mathrm{dil,tot}} = \frac{\tau_{\mathrm{oct}}}{\sigma^*} - a \cdot \left(\frac{\sigma_{\mathrm{m}}}{\sigma^*}\right)^2 - b \cdot \left(\frac{\sigma_{\mathrm{m}}}{\sigma^*}\right) \tag{17}$$

in a total stress formulation, and as

$$F_{\mathrm{dil,eff}} = \frac{\tau_{\mathrm{oct}}}{\sigma^*} - a \cdot \left(\frac{\sigma_m'}{\sigma^*}\right)^2 - b \cdot \left(\frac{\sigma_m'}{\sigma^*}\right) \tag{18}$$

in an effective stress form, where the effective stresses are obtained by means of the hypothetical depth-dependent pore pressure defined in Eq. (14). The octahedral shear stress is given as

$$\tau_{\mathrm{oct}} = \sqrt{\frac{2}{3}J_2} = \frac{\sqrt{2}}{3}\bar{\sigma} \tag{19}$$

in both criteria (deviatoric measure). Again, violation of the criterion is implied for $F_{\mathrm{dil}} \geq 0$.

2.2.3. Numerical methods

The quasi-static creep analyses were performed using OGS-6 [31, 51], an open-source finite element simulation platform. Standard linear finite elements were used. The global equilibrium iteration as well as the local stress update procedures are based on a consistent linearization in the context of a Newton-Raphson procedure [40, 41]. The non-linear absolute tolerance of the global Newton-Raphson scheme was set to 1×10^{-10}, the absolute tolerance of local Newton-Raphson stress-integration scheme to 1×10^{-12}.

Due to the large computational domain sizes encountered in the simulations of the horizontal caverns, an MPI parallelization was used to speed up the simulation. For that purpose, the code was compiled and tested on the Sunway TaihuLight Cluster equipped with nodes each having 2 E5-2680V3 processing cores [52]. Some initial test simulations were also conducted at the JUWELS supercomputer at the Jülich Supercomputing Centre.

The internal communication speed of each node is higher than the communication speed between the nodes. Thus, the following simulation strategy was chosen. Each cavern model is run within one node with minimum communication cost. For that purpose, each cavern model was decomposed into 12 partitions to utilize the 12 compute cores of the given node. In turn, the 12 cavern models representing different cavern lengths were run simultaneously on different nodes. Based on estimates derived from early phase simulations, the speed-up achieved was at least a factor of 7, though this number should not be considered an exact performance measure.

3. Results of geomechanical simulation of horizontal salt caverns

3.1. Creep deformation of horizontal cavern

According to the investigation, the vertical in-situ stress of the formation in Jintan is around 23.87 MPa, and the horizontal stress factor is 1.0 [53, 32]. Therefore, a matching isotropic initial stress state is assumed here. To reproduce the actual stress state in our simulation, gravitational effects were considered in the entire model, and an overburden pressure of 12.64 MPa was applied on the top surface of the FEM model, cf. Figure 3. The internal gas pressure is usually chosen according to the depth of the cavern top and generally is set to a range of 0.3 to 0.8 of the vertical stress at the cavern top [21, 54]. Thus, the internal gas pressure range could be 7.2 MPa to 19.1 MPa in the present case. The primary focus of this study is the basic mechanical behavior of horizontal caverns with different lengths. Three values were investigated for the internal pressure: a low, an average, and a high internal pressure, with values 7.2 MPa, 13.15 MPa and 19.1 MPa, respectively, see Table 2. The entire simulation period covered 30 years, which is a typical designed service life of a salt cavern gas storage. The fast initial unloading of salt cavern was modelled as instantaneous and thus occurred in a practically elastic fashion. The simulation results of displacement distribution of salt cavern with length 600 m and 900 m after 30 years of operation are shown in Figure 4. The largest displacements occur at the top-center protrusion, the largest deformation location mostly depends on the length of the cavern in relation to its other dimensions.

Operating pressure	Low	Mid	High
Value in MPa	7.2	13.15	19.1

Table 2: Typical operating pressure of horizontal cavern

The creep displacement and volume change of the cavern with a length of 600 m are shown in Figure 5. The volumetric convergence representing the averaged volume loss of the entire salt cavern is a crucial criterion in design, as

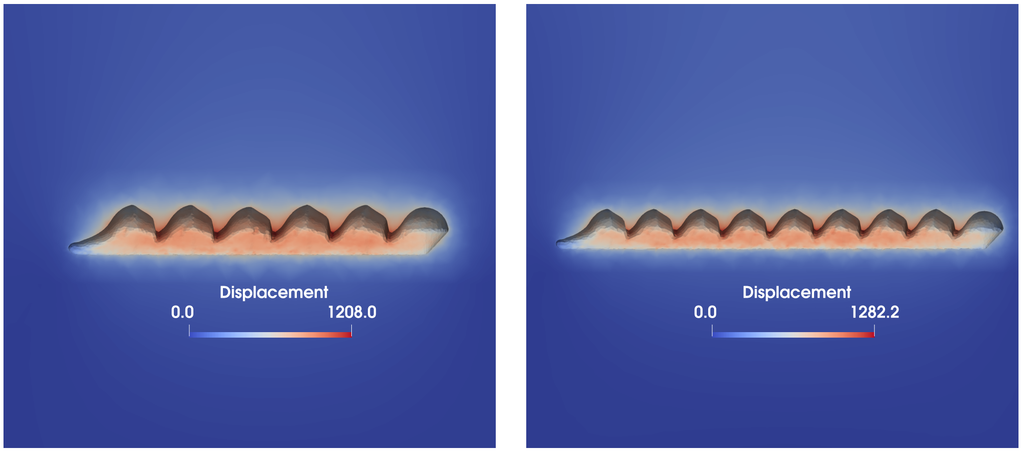

(a) Length 600 m (b) Length 900 m

Figure 4: Displacement magnitude after 30 years of stationary creep for the 'mid' pressure scenario. Displacements in mm.

described elsewhere [21]. Under "Low" internal pressure, both the magnitude of the maximum displacement and the volume loss are the most severe. What appears as primary creep and secondary creep stages is a consequence of the stress-dependence of the creep law in connection with stress redistribution around the cavern. The material model itself only considers stationary creep. The deformation cavern in the "High" pressure scenario, where pressure is close to lithostatic, is consequently very small. Even in the "Low" internal pressure scenario, the volume change after 30 years of operation is 14 % for the chosen parameters, much lower than the stipulated level 30 % [21] . This further demonstrates the need for more detailed assessments to demonstrate the feasibility of this multi-step horizontal salt cavern storage.

The effect of cavern length is illustrated in Figure 6. Peak displacements slightly increase with increasing length with a variation below 30 %. When increasing the dissolution length of the horizontal cavern, the maximum displacement and average deformation (volumetric convergence) do not increase linearly. Once the horizontal length exceeds 600 m, i.e. 5 to 6 times the cross-sectional diameter, the maximum deformation plateaus and does not change appreciably afterwards. One can think of this phenomenon as the cavern transitioning to a tunnel with a large cross sectional area. In the interior regions, the cavern's deformation is then determined by its cross section in a

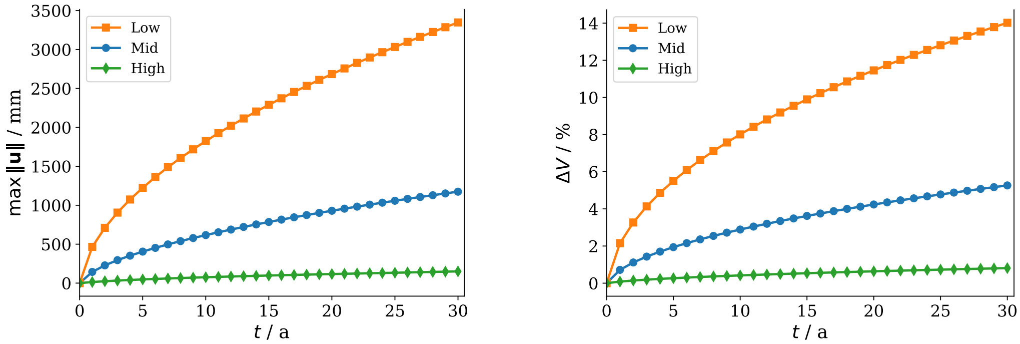

(a) Maximum creep displacement

(b) Cavern convergence

Figure 5: Deformation of salt cavern with length of 600 m for different internal pressure.

quasi-2D manner.

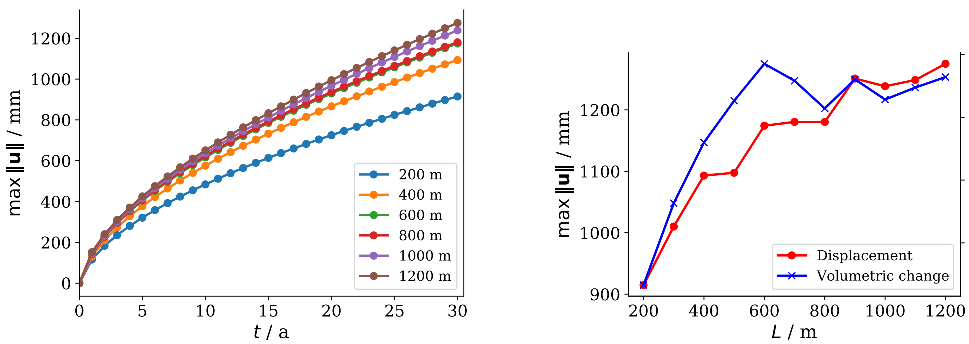

(a) Creep displacement at top-center protrusion

(b) Deformation vs length of cavern

Figure 6: Maximum displacement and volume loss depending on cavern length for the 'mid' pressure case

3.2. Integrity criteria

Barrier integrity is evaluated by applying the fluid pressure criterion and the dilatancy criterion, the latter both in total and effective stress form, where positive values indicate a violation of the criterion, termed failure here for short. The failure zones of the typical cavern model are shown in Figure 7 – Figure 9. The cavern stress status does not exceed the dilatancy criterion in total stress formulation for any of the pressures after 30 years creep, while for the fluid pressure criterion and effective stress-based dilatancy criterion, failure zones exist at low cavern pressures and decrease when the pressure increases, because the internal pressure balances the excavation-induced unloading and decreases deviatoric stresses. The failure zones marked by the fluid pressure criterion affect the largest volume. The size effect of the horizontal cavern is illustrated in Figure 10a, showing an an increasing failure zone extent with increasing cavern length. When expressing the failure zone normalized to cavern length (Figure 10b), the results dramatically show that the failure volume of per unit horizontal length remains roughly steady, and even reduces slightly as the cavern approaches tunnel character.

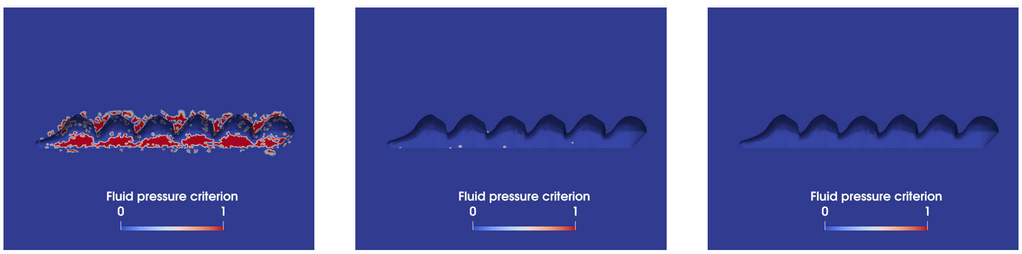

(a) Low (b) Mid (c) High

Figure 7: Failure zone following the fluid pressure criterion in the surrounding rock for a cavern length of 600 m.

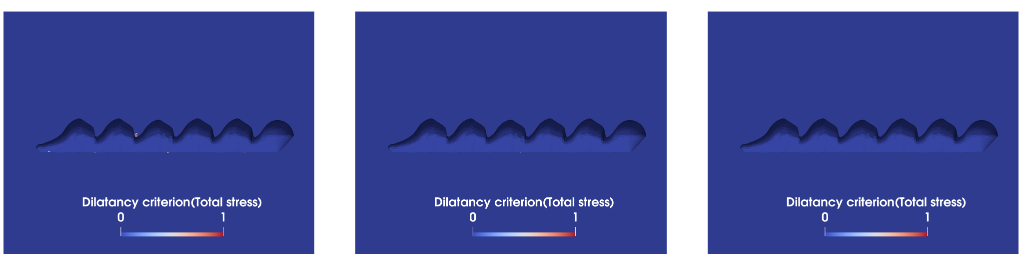

(a) Low (b) Mid (c) High

Figure 8: Failure zone following the dilatancy criterion (total stress) in the surrounding rock for a cavern length of 600 m.

The time effect of indicated cavern failure zones can be seen in Figure 11: the failure zone volume of the fluid pressure criterion and effective stress-based dilatancy criterion increases due to creep and subsequent stress redistribution at the first 2 years, and then reduces, due to the stress release,

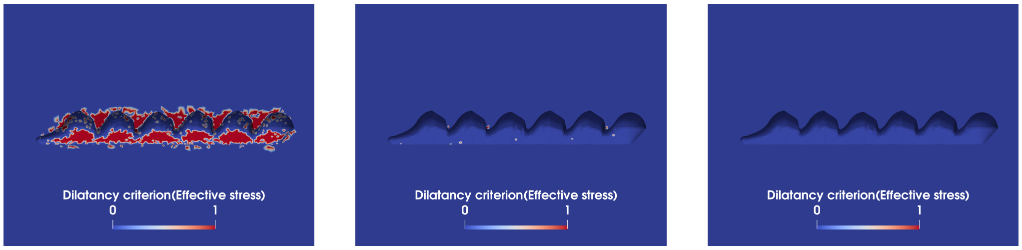

(a) Low (b) Mid (c) High

Figure 9: Failure zone following the dilatancy criterion (effective stress) in the surrounding rock for a cavern length of 600 m.

likely due to deviatoric stress relaxation due to salt creep. This phenomenon reflects the apparent primary and secondary creep behavior discussed earlier. During the steady-state creep phase, the failure volume increase slows down but has not yet levelled off after the 30 years simulated here. The failure zone volume of the total stress-based dilatancy criterion appears slightly at the initial 2 years creep stage, and then vanishes. In addition to the failure zone volume calculation in Figure 11, the parallel numerical models simulated with realistic shape facilitate a closer evaluation of the failure zone distribution of different stages. The profiles in Figure 12 illustrate the effective-stress based dilatancy zone distribution as it changes from the initial state during the subsequent 30 years. At the initial step of the simulation (cavern dissolution completed), results show the dilatancy zone covering the immediate vicinity of the cavern. After decades of creep, the affected area is redistributed and moves from some areas along the wall towards the cavern roof. Other regions, previously subjected to high deviatoric stresses, transition from violating the dilatancy criterion back to complying with it associated with a relaxation of the high deviatoric stresses. In other words, not only does the volume potentially affected by damage change, but also the location of the affected regions shifts due to stress redistribution. The area where dilatant damage accumulated during the creep phase coincided with the irregular "bulge" shape caused by the control of the cavern dissolution process.

3.3. Limitations and future work

Future work should take into account some extensions of the current analysis methodology. Firstly, more advanced material models [48, 40] might be

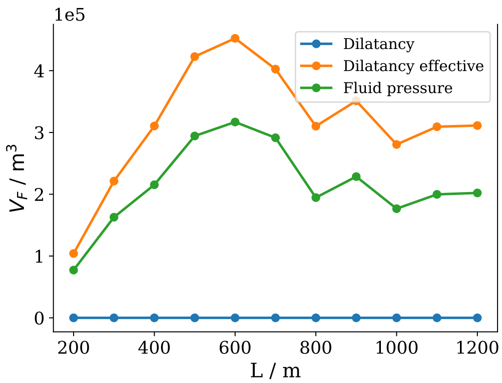

(a) Failure volume vs. cavern size

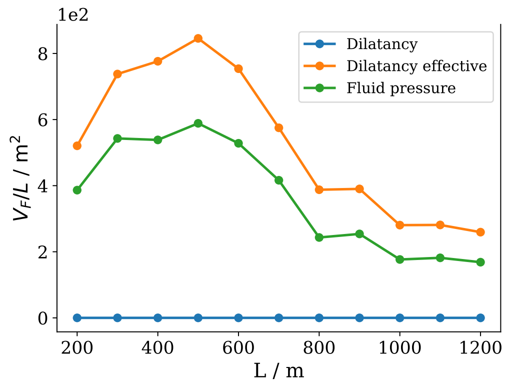

(b) Failure volume per unit length vs. cavern size

Figure 10: Failure under low pressure vs. cavern length (left) and normalized to cavern length (right).

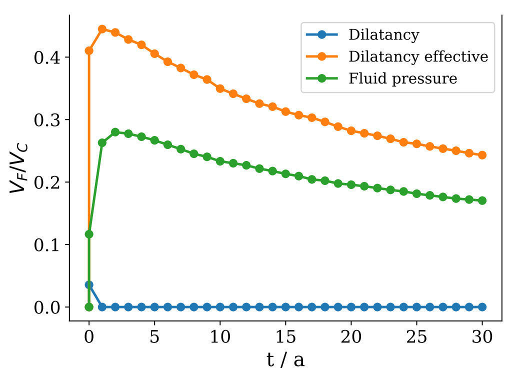

Figure 11: Failure volume vs. creep time (600 m, Low)

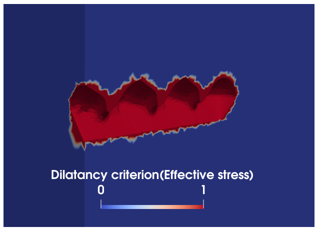

(a) Initial step

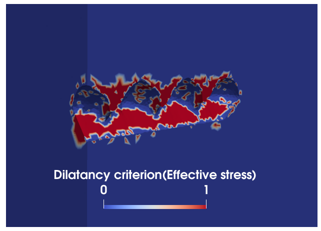

(b) 15 years creep

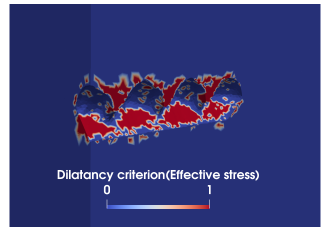

(c) 30 years creep

Figure 12: Creep effects on the effective dilatancy zone of surrounding rock for a cavern length of 600 m under Low pressure.

considered which account for primary, secondary and tertiary creep along with an explicit calculation of dilatancy. Particular extensions for bedded salt may also be considered [55]. This will allow for the modelling of storage operations including charging and discharging of the cavern storage. Depending on the frequency of this cyclic loading, thermal effects due to gas thermodynamics may have to be considered in the model (thermo-mechanical analyses). If fluid effects at the boundary to the overburden or infiltration of the storage medium into the cavern's contour are of interest, hydraulic-mechanical coupling may also be considered. Finally, the influence of interfaces between rock types and associated with insoluble interlayers can be considered for more realistic stress fields. Such interfaces and the likelihood of encountering them with increasing size of the engineered structure will have to be included in an actual safety assessment for a given site. Looking at the solution mining itself, the step distance during construction of the multi-step cavern, and the injection flow rate during dissolution might influence the shape and thus stability of the cavern as well, and might be discussed in subsequent studies.

4. Conclusion

The impact of the length of a horizontal cavern on its geomechanical behaviour is analyzed, using the solution mining model M-SHSCLS to obtain realistic cavern geometries with different length, and using OpenGeoSys to conduct the mechanical analysis. The conclusions are as follows:

1. Three typical internal pressure values, 7.2 MPa, 13.15 MPa and 19.1 MPa, were investigated in the present analysis ranging from 30 to 80 % of the

lithostatic stress. Even in the mechanically most challenging setting of low internal pressure, the volume change after 30 years of operation was limited to 14 %. The horizontal cavern volume change thus remains below the design criteria. It further demonstrates the principal feasibility of this kind of multi-step horizontal cavern. Note that this number is an estimate based on the chosen parameters and modelling strategy and may thus be subject to variation once more refined analyses are performed.

2. With the increase of the horizontal length, the peak deformation first increases, but begins to converge after the horizontal length exceeds 600 m, i.e. 5 to 6 times the cross-sectional diameter. Potentially damaged zones are evaluated by applying the fluid pressure criterion and the dilatancy criterion. The total volume affected by potential damage increases with increasing horizontal length, while the failure volume zone per unit length remains roughly steady, and even reduces slightly as the cavern approaches tunnel character. Thus, it can be concluded that increasing the horizontal length to longer than 5 to 6 times the designed cross-sectional diameter is in principle feasible to access large storage volumes.
3. Failure tends to accumulate at the lower parts of the cavern roof caused by the uneven dissolution. It indicates that irregular shapes could induce dilatancy-induced unstable cavern wall sections and confirms the need to take into account realistic geometires. Therefore, the construction method and shape control technology are suggested to be improved to realize a longer, and more regularly shaped horizontal cavern.

Acknowledgments

This research was funded in part by Basic Science Center Program for Multiphase Evolution in Hyper-gravity of the National Natural Science Foundation of China (No. 51988101), the Fundamental Research Funds for the Central Universities (No. 2020QNA4020), the Federal Ministry of Education and Research Germany (BMBF) under Grant No. 03ZZ0721H (H2-UGS project), Grant No. 03G0899D (GeomInt-2 project) and NSFC General Program(No. 51774295). The authors gratefully acknowledge the support of the Project Management Jülich (PtJ). The authors gratefully acknowledge the Earth System Modelling Project (ESM) for funding this work by providing computing time on the ESM partition of the supercomputer JUWELS at the Jülich Supercomputing Centre (JSC).

CRediT author statement

JL: Conceptualization, Investigation, Methodology, Writing – original draft. **NZ:** Software, Investigation, Formal analysis, Methodology, Writing – original draft. **WX:** Conceptualization, Writing – Review & Editing. **DN:** Software, Writing – Review & Editing. **TF:** Software, Writing – Review & Editing. **YC:** Supervision, Funding acquisition. **TN:** Methodology, Supervision, Software, Writing – Review & Editing, Funding acquisition.

Conflict of interest

The authors declare no potential conflict of interests.

References

[1] H. Kazemi, F. Jessen, Mechanism of Flow and Controlled Dissolution of Salt in Solution Mining, Society of Petroleum Engineers Journal 4 (04) (1964) 317–328.

[2] J. Li, X. Shi, C. Yang, Y. Li, T. Wang, H. Ma, Mathematical model of salt cavern leaching for gas storage in high-insoluble salt formations, Scientific Reports 8 (1) (2018).

[3] J. Wallbrecht, Underground gas storage, International Gas Union, Report of Working Committee 2 (2006).

[4] G. Wu, Y. M. Wei, C. Nielsen, X. Lu, M. B. McElroy, A dynamic programming model of China's strategic petroleum reserve: General strategy and the effect of emergencies, Energy Economics 34 (4) (2012) 1234–1243.

[5] N. Zhang, X. Shi, T. Wang, C. Yang, W. Liu, H. Ma, J. J. Daemen, Stability and availability evaluation of underground strategic petroleum reserve (SPR) caverns in bedded rock salt of Jintan, China, Energy 134 (2017) 504–514.

[6] A. Ozarslan, Large-scale hydrogen energy storage in salt caverns, International Journal of Hydrogen Energy 37 (19) (2012) 14265–14277.

[7] N. Böttcher, U.-J. Görke, O. Kolditz, T. Nagel, Thermo-mechanical investigation of salt caverns for short-term hydrogen storage, Environmental Earth Sciences 76 (3) (2017) 98. doi:10.1007/s12665-017-6414-2.

[8] W. Liu, Z. Zhang, J. Chen, J. Fan, D. Jiang, D. Jjk, Y. Li, Physical simulation of construction and control of two butted-well horizontal cavern energy storage using large molded rock salt specimens, Energy 185 (2019) 682–694.

[9] A. Soubeyran, A. Rouabhi, C. Coquelet, Thermodynamic analysis of carbon dioxide storage in salt caverns to improve the Power-to-Gas process, Applied Energy 242 (August 2018) (2019) 1090–1107.

[10] X. Shi, Y. Li, C. Yang, Y. Xu, H. Ma, W. Liu, G. Ji, Influences of filling abandoned salt caverns with alkali wastes on surface subsidence, Environmental Earth Sciences 73 (11) (2015) 6939–6950.

[11] J. Ślizowski, L. Lankof, Salt-mudstones and rock-salt suitabilities for radioactive-waste storage systems: Rheological properties, Applied Energy 75 (1-2) (2003) 137–144.

[12] B. Sedaee, M. Mohammadi, L. Esfahanizadeh, Y. Fathi, Comprehensive modeling and developing a software for salt cavern underground gas storage, Journal of Energy Storage 25 (July) (2019) 100876.

[13] P. Bérest, J. Bergues, B. Brouard, J. G. Durup, B. Guerber, A salt cavern adandonment test, International Journal of Rock Mechanics and Mining Sciences 38 (3) (2001) 357–368.

[14] J. Li, Y. Tang, X. Shi, W. Xu, C. Yang, Modeling the construction of energy storage salt caverns in bedded salt, Applied Energy 255 (September) (2019).

[15] L. Jinlong, X. Wenjie, Z. Jianjing, L. Wei, S. Xilin, Y. Chunhe, Modeling the mining of energy storage salt caverns using a structural dynamic mesh, Energy 193 (2020) 116730.

[16] P. Li, Y. Li, X. Shi, K. Zhao, X. Liu, H. Ma, C. Yang, Prediction method for calculating the porosity of insoluble sediments for salt cavern gas storage applications, Energy 221 (2021) 119815. `doi:https://doi.org/10.1016/j.energy.2021.119815`.

[17] Y. Li, X. Chen, X. Shi, N. Zhang, C. Ma, C. Yang, Analysis of the plugging process of the leaking interlayer in a thin interbedded salt cavern gas storage of Jintan (China) by high-pressure grouting and potential applications, Journal of Natural Gas Science and Engineering 68 (June) (2019) 102918.

[18] G. Zhang, L. Wang, Y. Wu, Y. Li, S. Yu, Failure mechanism of bedded salt formations surrounding salt caverns for underground gas storage, Bulletin of Engineering Geology and the Environment 76 (4) (2017) 1609–1625. `doi:{10.1007/s10064-016-0958-3}`.

[19] C. Querio, Design and construction of solution-mined caverns for lpg storage, in: Solution Mining Research Institute's fall meeting, Minneapolis, Minn., Oct, -, 1980, pp. 12–15.

[20] J. Li, C. Yang, X. Shi, W. Xu, Y. Li, J. J. Daemen, Construction modeling and shape prediction of horizontal salt caverns for gas/oil storage in bedded salt, Journal of Petroleum Science and Engineering 190 (January) (2020) 107058.

[21] W. Liu, D. Jiang, J. Chen, J. J. Daemen, K. Tang, F. Wu, Comprehensive feasibility study of two-well-horizontal caverns for natural gas storage in thinly-bedded salt rocks in China, Energy 143 (2018) 1006–1019.

[22] T. Wang, C. Yang, H. Wang, S. Ding, J. Daemen, Debrining prediction of a salt cavern used for compressed air energy storage, Energy 147 (2018) 464–476. doi:https://doi.org/10.1016/j.energy.2018.01.071.

[23] J. Wan, T. Peng, R. Shen, M. J. Jurado, Numerical model and program development of TWH salt cavern construction for UGS, Journal of Petroleum Science and Engineering 179 (March) (2019) 930–940.

[24] J. Wan, T. Peng, M. J. Jurado, R. Shen, G. Yuan, F. Ban, The influence of the water injection method on two-well-horizontal salt cavern construction, Journal of Petroleum Science and Engineering 184 (June 2019) (2020) 106560.

[25] R. Thoms, R. Gehle, Feasibility of controlled solution mining from horizontal wells, Solution Mining Research Institute (1993).

[26] C. Yang, T. Wang, Y. Li, H. Yang, J. Li, D. Qu, B. Xu, Y. Yang, J. J. Daemen, Feasibility analysis of using abandoned salt caverns for large-scale underground energy storage in China, Applied Energy 137 (2015) 467–481.

[27] W. Xing, J. Zhao, Z. Hou, P. Were, M. Li, G. Wang, Horizontal natural gas caverns in thin-bedded rock salt formations, Environmental Earth Sciences 73 (11) (2015) 6973–6985.

[28] J. Li, X. Shi, S. Zhang, Construction modeling and parameter optimization of multi-step horizontal energy storage salt caverns, Energy 203 (2020) 117840. doi:https://doi.org/10.1016/j.energy.2020.117840.

[29] J. Chen, D. Lu, W. Liu, J. Fan, D. Jiang, L. Yi, Y. Kang, Stability study and optimization design of small-spacing two-well (SSTW) salt caverns for natural gas storages, Journal of Energy Storage 27 (January) (2020).

[30] W. Xing, J. Zhao, U. Düsterloh, D. Brückner, Z. Hou, L. Xie, J. Liu, Experimental study of mechanical and hydraulic properties of bedded rock salt from the Jintan location, Acta Geotechnica 9 (1) (2014) 145–151.

[31] L. Bilke, B. Flemisch, T. Kalbacher, O. Kolditz, R. Helmig, T. Nagel, Development of open-source porous-media simulators: principles and experiences., Transport in Porous MediaIn print (2019).

[32] T. Wang, J. Li, G. Jing, Q. Zhang, C. Yang, J. J. Daemen, Determination of the maximum allowable gas pressure for an underground gas storage salt cavern – A case study of Jintan, China, Journal of Rock Mechanics and Geotechnical Engineering 11 (2) (2019) 251–262.

[33] C. Geuzaine, J.-F. Remacle, Gmsh: A 3-D finite element mesh generator with built-in pre- and post-processing facilities, International Journal for Numerical Methods in Engineering 79 (11) (2009) 1309–1331. doi:10.1002/nme.2579.

[34] O. Kolditz, S. Bauer, L. Bilke, N. Böttcher, J.-O. Delfs, T. Fischer, U.-J. Görke, T. Kalbacher, G. Kosakowski, C. McDermott, et al., Opengeosys: an open-source initiative for numerical simulation of thermo-hydro-mechanical/chemical (thm/c) processes in porous media, Environmental Earth Sciences 67 (2) (2012) 589–599.

[35] C. Yang, J. J. Daemen, J. H. Yin, Experimental investigation of creep behavior of salt rock, International Journal of Rock Mechanics and Mining Sciences 36 (2) (1999) 233–242. doi:10.1016/S0148-9062(98)00187-9.

[36] U. Hunsche, A. Hampel, Rock salt — the mechanical properties of the host rock material for a radioactive waste repository, Engineering Geology 52 (3-4) (1999) 271–291. doi:10.1016/S0013-7952(99)00011-3.

[37] N. Cristescu, U. Hunsche, A Constitutive Equation For Salt, in: the 7th ISRM Congress, Aachen, 1991.

[38] E. Orowan, Zur Temperaturabhängigkeit der Kristallplastizität, Zeitschrift für Physik 102 (1-2) (1936) 112–118. `doi:10.1007/BF01336834`.
URL `http://link.springer.com/10.1007/BF01336834`

[39] O. Kolditz, H. Shao, W. Wang, S. Bauer (Eds.), Thermo-Hydro-Mechanical-Chemical Processes in Fractured Porous Media: Modelling and Benchmarking, Terrestrial Environmental Sciences, Springer International Publishing, Cham, 2015. `doi:10.1007/978-3-319-11894-9`.
URL `http://link.springer.com/10.1007/978-3-319-11894-9`

[40] T. Nagel, W. Minkley, N. Böttcher, D. Naumov, U.-J. Görke, O. Kolditz, Implicit numerical integration and consistent linearization of inelastic constitutive models of rock salt, Computers & Structures 182 (2017) 87–103. `doi:10.1016/j.compstruc.2016.11.010`.

[41] N. Zhang, T. Nagel, Error-controlled implicit time integration of elasto-visco-plastic constitutive models for rock salt, International Journal for Numerical and Analytical Methods in Geomechanics 44 (8) (2020) 1109–1127. `doi:10.1002/nag.3049`.

[42] T. Helfer, J. Bleyer, T. Frondelius, I. Yashchuk, T. Nagel, D. Naumov, The MFrontGenericInterfaceSupport project, Journal of Open Source Software 5 (48) (2020) 2003. `doi:10.21105/joss.02003`.

[43] R. de Borst, O. M. Heeres, A unified approach to the implicit integration of standard, non-standard and viscous plasticity models, International Journal for Numerical and Analytical Methods in Geomechanics 26 (11) (2002) 1059–1070. `doi:10.1002/nag.234`.

[44] W. Chen, G. Wu, Y. Dai, C. Yang, Stability analysis of abandoned salt caverns used for underground gas storage, Chinese Journal of Rock Mechanics and Engineering 25 (4) (2006) 848–854.

[45] C. Yang, T. Wang, Y. Li, H. Yang, J. Li, D. Qu, B. Xu, Y. Yang, J. J. Daemen, Feasibility analysis of using abandoned salt caverns for large-scale underground energy storage in China, Applied Energy 137 (2015) 467–481.

[46] P. Li, Y. Li, X. Shi, A. Zhao, S. Hao, X. Gong, S. Jiang, Y. Liu, Stability analysis of U-shaped horizontal salt cavern for underground natural gas

storage, Journal of Energy Storage 38 (June) (2021) 102541. doi:10.1016/j.est.2021.102541.
URL https://doi.org/10.1016/j.est.2021.102541

[47] E. K. Simo, M. Breustedt, N. Müller-Hoeppe, C. Missal, J. Stahlmann, Evaluation of the barrier integrity based on effective stresses using the dilatancy and fluid pressure criterion, Geotechnik 39 (4) (2016) 263–274.

[48] K. Khaledi, E. Mahmoudi, M. Datcheva, T. Schanz, Stability and serviceability of underground energy storage caverns in rock salt subjected to mechanical cyclic loading, International Journal of Rock Mechanics and Mining Sciences 86 (2016) 115–131. doi:10.1016/j.ijrmms.2016.04.010.

[49] N. Cristescu, U. Hunsche, Time effects in rock mechanics, Wiley series in materials, modelling and computation, Wiley, 1998.

[50] H. Ma, C. Yang, Y. Li, X. Shi, J. Liu, T. Wang, Stability evaluation of the underground gas storage in rock salts based on new partitions of the surrounding rock, Environmental Earth Sciences 73 (11) (2015) 6911–6925. doi:10.1007/s12665-015-4019-1.

[51] OpenGeoSys website, www.opengeosys.org, accessed: 2020-05-16.

[52] National supercomputing center in wuxi website, http://www.nsccwx.cn/swsource/5d2fe23624364f0351459262, accessed 2021-01-11.

[53] X. Yin, C. Yang, J. Chen, Numerical simulation research on long-term stability of gas storage in Jintan salt mine, Rock and Soil Mechanics 27 (6) (2006) 869–874.

[54] K. L. Devries, K. D. Mellegard, G. D. Callahan, W. M. Goodman, Cavern Roof Stability for Natural Gas Storage in Bedded Salt, Tech. Rep. September 2002 (2005).

[55] Y.-P. Li, C.-H. Yang, J. J. K. Daemen, X.-Y. Yin, F. Chen, A new Cosserat-like constitutive model for bedded salt rocks, International Journal for Numerical and Analytical Methods in Geomechanics 33 (15) (2009) 1691–1720. doi:10.1002/nag.784.
URL https://onlinelibrary.wiley.com/doi/10.1002/nag.784